Diffraction anomalous fine-structure spectroscopy at beamline BM2 at the European Synchrotron Radiation Facility

H. Renevier,[a,b]*† S. Grenier,[a,c]‡ S. Arnaud,[a] J. F. Bérar,[a] B. Caillot,[a] J. L. Hodeau,[a] A. Letoublon,[a]† M. G. Proietti[d] and B. Ravel[e]

[a]Laboratoire de Cristallographie, Centre National de la Recherche Scientifique, BP 166, F-38042 Grenoble CEDEX 09, France, [b]Université Joseph Fourier, BP 53, F-38041 Grenoble CEDEX 09, France, [c]Department of Physics and Astronomy, Rutgers University, Piscataway, NJ 08854, USA, [d]Departamento de Física de la Materia Condensada, Instituto de Ciencia de Materiales de Aragón, CSIC-Universidad de Zaragoza, c. Pedro Cerbuna 12, 50009 Zaragoza, Spain, and [e]Center for Corrosion Chemistry and Engineering, Code 6134, Naval Research Laboratory, Washington, DC 20375, USA.
E-mail: hubert.renevier@cea.fr

Diffraction anomalous fine-structure (DAFS) spectroscopy uses resonant elastic X-rays scattering as an atomic, shell and site-selective probe that provides information on the electronic structure and the local atomic environment as well as on the long-range-ordered crystallographic structure. A DAFS experiment consists of measuring the Bragg peak intensities as a function of the energy of the incoming X-ray beam. The French CRG (Collaborative Research Group) beamline BM2-D2AM (Diffraction Diffusion Anomale Multi-longueurs d'Onde) at the ESRF (European Synchrotron Radiation Facility) has developed a state-of-the-art energy scan diffraction set-up. In this article the requirements for obtaining reliable DAFS data are presented and recent technical achievements are reported.

Keywords: diffraction; DAFS.

1. Introduction

Before entering into the technical details, a discussion of the interest in DAFS spectroscopy is merited. A DAFS experiment consists of measuring the elastic scattering intensity as a continuous function of the incoming X-ray beam energy in regions spanning absorption edges. It provides information about the chemical state and the local environment of the resonant atom (also known as the anomalous atom), like X-ray absorption fine-structure (XAFS) spectroscopy. In contrast to XAFS, however, it is a chemical-selective and site-selective spectroscopy. Like multiple-wavelength anomalous diffraction (MAD), DAFS provides a means of recovering the phase of the structure factor, which is important for solving the long-range average crystallographic structure.

Observation of X-ray DAFS was reported for the first time in the mid-1950s by Cauchois (1956). With a dispersive diffraction set-up using a wavelength-bent single crystal of mica, Cauchois observed intensity variations of the (002) reflection close to the Al *K* edge and suggested that they could be anomalous diffraction of the mica crystal. To our knowledge, no further contribution to developing the DAFS technique was made until the publications of Fukamachi *et al.* (1977) and Salem & Hall (1980). In 1982, Arndt *et al.* showed the possibility of performing anomalous dispersive diffraction measurements at synchrotron radiation sources for the phase determination of the structure factor (Arndt *et al.*, 1982). In 1987, Arcon *et al.* measured the Bragg reflectivity extended structure at the Cu *K* edge of a copper sulfate single crystal using an X-ray tube (Arcon *et al.*, 1987). The data clearly exhibited anomalous diffraction oscillations and a method to analyse them was proposed. Although these were pioneering experiments, attention was paid neither by the diffraction community nor by the absorption community to the measurement of diffraction intensity as a function of the energy near absorption edges. In 1992, Stragier *et al.* presented an elegant demonstration of the so-called DAFS spectroscopy on a copper single crystal (Stragier *et al.*, 1992). At the same time, Pickering *et al.* were measuring the DAFS spectra of powder Fe_3O_4 to extract site-selective spectra of Fe in the octahedral and tetrahedral sites (Pickering *et al.*, 1993*a*,*b*). Later, several groups applied the method at synchrotron radiation facilities with both monochromatic and dispersive optics to study thin films, multi-layers, powders and single crystals. In this paper we present the set-up and technical requirements of the DAFS experiment. The reader can find extensive information about DAFS and anomalous diffraction in the review article by Sorensen *et al.* (1994) and more recently by Hodeau *et al.* (2001). The article by Proietti *et al.* (1999) develops the analysis of the extended-DAFS (EDAFS), *i.e.* the portion of the DAFS spectrum above the absorption energy.

2. Elementary background

2.1. The complex atomic scattering factor

Consider the scattering of an atom *A* in a solid sample. Near an absorption edge the elastic scattering of that atom is expressed as the sum of the energy-independent Thomson scattering, $f_{0A}(\mathbf{Q})$, and the complex resonant (anomalous) scattering,

$$f_A(\mathbf{Q}, E) = \boldsymbol{\varepsilon} \cdot \boldsymbol{\varepsilon}' f_{0A}(\mathbf{Q}) + f'_A(E, \mathbf{k}, \mathbf{k}', \boldsymbol{\varepsilon}, \boldsymbol{\varepsilon}') + i f''_A(E, \mathbf{k}, \mathbf{k}', \boldsymbol{\varepsilon}, \boldsymbol{\varepsilon}'), \quad (1)$$

where $\mathbf{Q} = \mathbf{k}' - \mathbf{k}$ is the scattering vector, $\mathbf{k}$ and $\mathbf{k}'$ are the incident and outgoing wavevectors, and $\boldsymbol{\varepsilon}$ and $\boldsymbol{\varepsilon}'$ are the polarization vectors of the incident and outgoing beams (unitary vectors), respectively (Sakurai, 1967; Blume, 1985; Cohen-Tannoudji *et al.*, 1988). Within the dipole–dipole approximation, the resonant scattering depends only on polarization and energy. As a general rule, the complex resonant scattering is not a scalar and can be expressed as

$$f'_A(E, \boldsymbol{\varepsilon}, \boldsymbol{\varepsilon}') + i f''_A(E, \boldsymbol{\varepsilon}, \boldsymbol{\varepsilon}') = \boldsymbol{\varepsilon}'[D]\boldsymbol{\varepsilon},$$

where $[D]$ is a tensor of rank 2, whose symmetry is given by the point-group symmetry of the crystallographic site *A* (Templeton & Templeton, 1980; Dmitrienko, 1983). In the forward-scattering limit, the optical theorem (Cohen-Tannoudji *et al.*, 1973) shows that the imaginary part of the elastic resonant scattering is proportional to the total cross section,

$$f''_A(\mathbf{Q} = 0, E) = \frac{E}{2hcr_0}\sigma_{A,\text{total}}, \quad (2)$$

where $\sigma_{A,\text{total}}(E) = \sigma_{\text{elastic scatt}} + \sigma_{\text{abs}}$ and $r_0 = q^2/4\pi\varepsilon_0 mc^2$ is the classic electron radius. The absorption coefficient $\mu_A(E) = N_A\sigma_{A,\text{total}}(E)$, where N_A is the number of atoms *A* per volume unit, is the quantity measured by XAFS spectroscopy. Causality implies that f'_A (dispersion) and f''_A (absorption) are not independent, but rather related by the Kramers–Kronig transforms, as shown in Fig. 1. The virtual

† Present address: Commissariat à l'Energie Atomique, Département de Recherche Fondamentale sur la Matière Condensée, SP2M/NRS, 17 Rue des Martyrs, 38054 Grenoble CEDEX 9, France.
‡ Present address: Department of Physics, Brookhaven National Laboratory, Upton, NY 11973, USA.

intermediate state of the resonant-scattering process corresponds to an atom with a core hole and a virtual photoelectron in an atomic-like electronic state or in the continuum. Similar to X-ray absorption, the energy dependence above the Fermi level of the electronic density is shaped and modulated by the local atomic environment of the resonant atom. The factors f'_A and f''_A take into account the transition to intermediate states; for convenience, in the extended region, they can be split into 'smooth' and oscillatory parts, *i.e.*

$$f'_{Aj} = f'_{0A} + \Delta f''_{0A}\chi'_{Aj},$$
$$f''_{Aj} = f''_{0A} + \Delta f''_{0A}\chi''_{Aj},$$

where f'_{0A} and f''_{0A} are the resonant scattering terms of an isolated atom A, $\Delta f''_{0A}$ represents the contribution of the resonant scattering to f''_{0A}, and χ'_{Aj} and χ''_{Aj} are the fine-structure oscillations.

2.2. Selectivity

Unlike XAFS, DAFS spectroscopy is site selective because it measures the X-ray scattering and thus takes advantage of the wave interference to select a subset of atoms in the sample. For the sake of clarity, consider a centrosymmetric periodic structure [the general case is considered by Meyer *et al.* (1998) and Proietti *et al.* (1999)]. The scattering structure factor is

$$F \propto \sum_j m_j c_j \exp(-M_j Q^2) f_j(\mathbf{Q}, E) \cos(\mathbf{Q} \cdot \mathbf{r}_j), \qquad (3)$$

where the vector $\mathbf{r}_j$ gives the atomic position in the cell, and m_j, c_j and $\exp(-M_j Q^2)$ are the multiplicity, occupation and Debye–Waller factors, respectively. The scattered intensity is then proportional to the squared modulus of the structure factor. The summation runs over all atoms in the unit cell that are not related through the center of symmetry. The site selectivity is given by the term $\cos(\mathbf{Q} \cdot \mathbf{r}_j)$, the value of which depends on the dot product of the momentum-transfer vector with the position of atom j in the cell. Because of this, DAFS may distinguish the valence and local environment of atoms of the same atomic number located on different crystallographic sites. This has been used, for example, to recover the Fe scattering anomalous terms of the tetrahedral and octahedral sites in magnetite (Pickering *et al.*, 1993*a*), the local environment of Cu1 and Cu2 sites in the superconductor $YBa_2Cu_3O_7$ (Cross *et al.*, 1997; Cross, Newville *et al.*, 1998), and the interface structure of an Ir/Fe superlattice (Renevier *et al.*, 1997). In the special case of magnetite, there exist Bragg reflections strictly sensitive either to the octahedral or tetrahedral sites and without contribution from the other site. To apply site selectivity and recover site-selective oscillations, the long-range-ordered average crystallographic structure must be known precisely. It is well known that multiwavelength anomalous diffraction (MAD) provides valuable information for solving the crystallographic structure (see, for instance, Hendrickson, 1985). Another useful application of DAFS is spatial selectivity. Information about a material embedded in another or which coexists with others can be obtained by measuring the DAFS spectra of the Bragg peaks of that material. Typical examples are thin films having one or more atomic species in common with the substrate and/or buffer (see examples in Hodeau *et al.*, 2001). More recently, DAFS has been applied to nanostructures (Grenier, Proietti *et al.*, 2002); in these cases, XAFS experiments in fluorescence mode would not allow discrimination of signals from heterostructures with a common element.

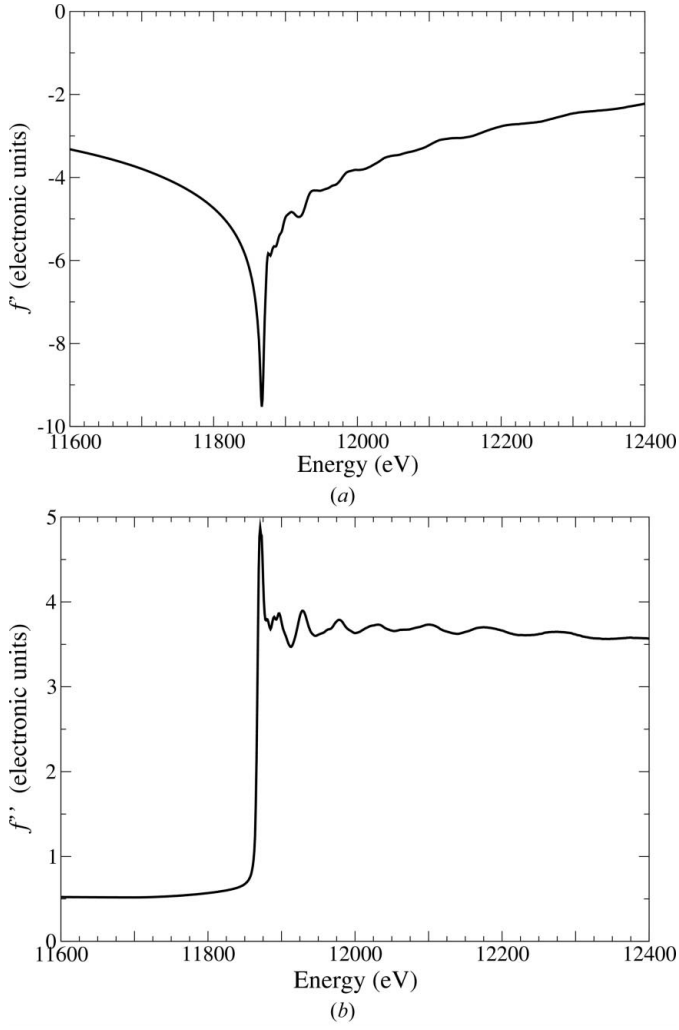

Figure 1
Experimentally determined (*a*) f'_{As} and (*b*) f''_{As}, the real and imaginary resonant scattering of As atoms in InAs bulk, respectively. The f''_{As} spectrum was obtained from an absorption measurement of an InAs powder using equation (2). f'_{As} is the Kramers–Kronig transform of f''_{As} calculated using the program *DIFFKK* (Cross, Newville *et al.*, 1998). The fine-structure oscillations provide information about the local atomic environment of the resonant atom.

2.3. Polarization dependence

As for XAFS, DAFS spectra depend on the X-ray beam polarization direction. For X-ray absorption, the crystallographic point group governs that dependence. For instance, the absorption is isotropic for a cubic point group even if the site symmetry of the absorber is not (Brouder, 1990). In the case of DAFS, the situation is quite different because of the interference mechanism. The polarization of the incoming and outgoing X-ray beams must be taken into account. *Via* virtual multipole transitions (mainly dipolar, quadrupolar or an interference of both), the energy dependences in σ–σ and σ–π channels (see §5.1 and Fig. 9) upon the incoming X-ray beam energy as well as upon the azimuthal angle (corresponding to a rotation about the scattering vector) can reveal the anisotropy of the susceptibility tensor (ATS) (Dmitrienko, 1983; Templeton & Templeton, 1980). The anisotropy is due to, for instance, *d*-orbital ordering (Murakami *et al.*, 1998), distortion ordering (García *et al.*, 2000) or charge ordering (Grenier, Toader *et al.*, 2002). Regarding structural analysis, the polarization dependence may be used as in X-ray absorption. For instance, in strained thin films or superlattices of materials which are cubic in the bulk, the interfaces may be non-cubic on the atomic scale. In that case, it is worth measuring DAFS spectra with the polarization of the incoming beam in and out of the

growth plane to probe in-plane and out-of-plane local distortions (Grenier, Proiettei *et al.*, 2002).

3. Energy-scan diffraction

The DAFS experiment is time-consuming since intensity oscillations of several Bragg reflections must be collected as a function of energy over a few hundred eV with a typical energy resolution of 1 eV, and sometimes require measurement of tiny diffraction-intensity variations. This is the reason why the techniques for experimental set-up and data collection are still under development. We report on the progress of the energy-scan diffraction with optics for delivering a monochromatic beam at beamline BM2-D2AM at the ESRF. In this mode the intensity of a Bragg reflection is collected as a function of the energy given by the Bragg angle of the monochromator crystal and is tuned step-by-step through the absorption edge of one of the atomic species in the sample. The requirements of the experiment are to measure the intensities *versus* the energy as fast as possible, with a monitor-corrected signal-to-noise ratio as high as 1000 or more (comparable to a typical XAFS experiment) and without distortions of the spectra. These requirements turn out to be a challenge for diffraction experiments. For that purpose, we use a fixed-exit diffraction beamline with an XAFS monochromator coupled to a diffractometer both having high-precision movement ($<0.001^\circ$). Beamline BM2-D2AM was built for using the light emitted by a bending magnet and is dedicated to anomalous-scattering experiments (Ferrer *et al.*, 1998). The beamline optics consist of a double-crystal channel-cut geometry, water-cooled monochromator and two 1.2 m-long platinum-coated Si mirrors [a schematic representation is given by Ferrer *et al.* (1998), Figs. 1 and 6]. The two mirrors are used for harmonic rejection, for vertical focusing and for vertical stability of the incoming X-ray beam at the sample position when changing the X-ray energy. The first mirror, which is upstream of the monochromator, also removes part of the heat load. The second crystal of the monochromator, usually Si(111), is mounted on a bender (Hazemann *et al.*, 1995) providing dynamic sagittal focusing. The smallest spot size at the focal point that can be delivered with the optics is 100 µm (horizontal) by 100 µm (vertical). A seven-circle diffractometer allows diffraction measurement in the vertical and horizontal planes and is suitable for polarization-dependent DAFS experiments. A crystal analyser, a Displex cryostat, a furnace and spherical beryllium vacuum enclosures are also available. It is worth emphasizing that reliable DAFS spectra are obtained provided that the beam size and position at the sample position (usually the focal point) are very stable over the energy range covered by the energy scan (about 1 keV). This implies perfect alignment of the optics, including dynamic sagittal focusing and tuning of the second crystal of the monochromator.

3.1. Maximum-intensity measurements

Since integrating reflection profiles at each energy and at several diffraction vectors is time-consuming, much effort has been put into performing the data collection by measuring only the maximum intensity of the Bragg peak as a function of energy. This allows the contribution of the fluorescence signal of the sample to be minimized, thus maximizing the fraction of diffracted photons measured at the diffraction detector. The measurement of the maximum of the diffracted intensity provides results identical to the integration measurement provided that the rocking-curve reflection profile is regular, as with thin films, superlattices and heterostructures. With bulk material or powder, a drastic change in the absorption length may lead to profile variations above the absorption edge. The peak profile depends on the mosaicity, the vertical beam divergence and the beam coherence. In that sense, the high beam collimation and coherence produced by third-generation insertion-device sources may be a concern. Since the mechanical precision and stability of all motors is necessarily limited, we developed a feedback control of the sample rocking-angle position (based on a sample holder that rocks the sample around the ω axis, see Fig. 2*a*) for measuring the maximum intensity (Cross, Elam *et al.*, 1998; Blanco, 1998; Grenier, 2001). The idea is to measure a quantity that is proportional to the derivative of the Bragg peak profile. At the low- and high-angle sides of the peak maximum the derivative is positive and negative, respectively, whereas at the maximum it is equal to zero. The derivative is then used to correct the ω angle in order to have the maximum intensity in the diffraction detector. When the derivative is equal to zero, the sample angle position is stable. Fig. 2(*b*) shows a scheme of the set-up developed at BM2-D2AM. The diffraction signal I_d is modulated by a reference sine signal rocking the sample holder and delivered by the lock-in amplifier (EG&G instruments, 7220 DSP) and fed into the lock-in input. The output is then given by

$$I_{\rm out} = (1/T)\, I_{\rm d}[\omega_0 + \Delta\omega \sin(\Omega t + \varphi)] \sin(\Omega t)\ {\rm d}t,$$

where $T = 2\pi/\Omega$ is the period of the oscillation and φ is the phase shift between I_d and the reference signal that is set to 180°. For amplitude modulations smaller than the full width at half-maximum

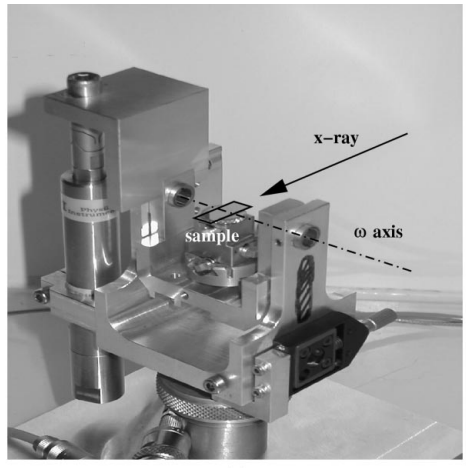

(*a*)

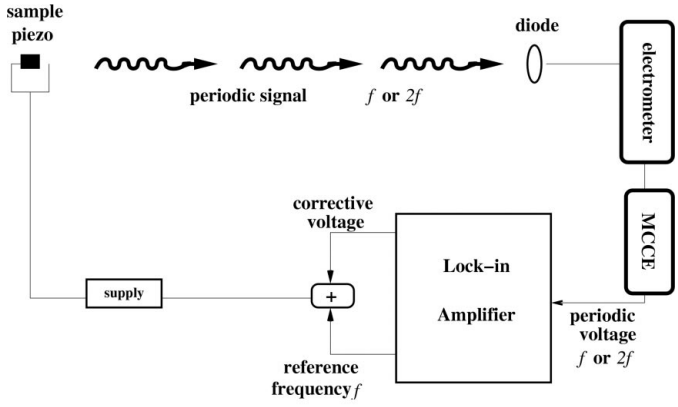

(*b*)

Figure 2
(*a*) Photograph of the rocking-sample holder developed at beamline BM2-D2AM. One can see the shiny surface of a GaAsP sample on the goniometer head. (*b*) Schematic of the feedback set-up.

(FWHM), it can be easily shown with a Taylor expansion of the diffracted intensity to first order that

$$I_{\rm out} \simeq (1/T)\int I_{\rm d}(\omega_0)\sin(\Omega t+\varphi)\ {\rm d}t + (1/T)\int\left[({\rm d}I_{\rm d}/{\rm d}\omega)\Delta\omega\sin(\Omega t+\varphi)\right]\sin(\Omega t)\ {\rm d}t. \quad (4)$$

The first term is equal to zero, whereas the second is proportional to $({\rm d}I_{\rm d}/{\rm d}\omega)\Delta\omega\cos\varphi$. A piezoelectric transducer (PI P-843.40) produces oscillations with amplitudes $\Delta\omega = 0.0167^\circ\ {\rm V}^{-1}$ and frequencies in the range 10–20 Hz. By compensating for the mechanical imperfections, the feedback control ensures measuring the maximum intensity of the ω profile as a function of the energy. It leads to a significant improvement of the signal-to-noise ratio and reduction of the low-frequency distortion of the spectra. Future improvements of this device include rocking the sample in arbitrary orientation and its implementation in high- and low-temperature sample environments. The feedback has broadened the application of the maximum-intensity measurement procedure to very narrow ω profiles, *i.e.* with a FWHM of the order or less than 0.01° in an ω scan.

3.2. Integration of the Bragg peak profile

In the case of mosaicity and/or domains, which introduce irregular reflection shapes (Vacínová *et al.*, 1995), or strong absorption (Bos, 1999) that modifies the Bragg peak profile when crossing the absorption edge, an ω scan (perpendicular to the diffraction vector) or an ω–2θ scan (along the diffraction vector) is mandatory for integrating the peak profile. To reduce the measurement time, a flying ω scan is performed at each energy step together with a counting on both sides of the peak to measure the background, including the sample fluorescence. In practice, the counting is triggered by the ω motor and the integrated intensity is the total number read by the counting crate during the time elapsed by the motor movement. This procedure is time-consuming and the ratio of diffracted intensity to the background signal is inherently much smaller compared with the maximum intensity measurement.

3.3. Experimental set-up and procedure

Our purpose is to obtain DAFS with a data quality comparable to the quality of typical XAFS data, thus making DAFS attractive to the XAFS community. This means that the diffraction is to be measured with a high signal-to-noise ratio as a function of the energy (at least 1000) and without any distortions. The experimental diffraction set-up (Fig. 3) consists of entrance slits, attenuators and a monitor (I_0), all in a vacuum environment. The sample, mounted on a seven-circle diffractometer, the scattering slits and the detector slits all lie outside the vacuum. As for an XAFS experiment, the incoming beam must be carefully monitored. This is done by measuring the fluorescence signal emitted by a 4 µm-thick 99.6%-pure Ti foil mounted in a vacuum and at 45° with respect to the beam path. Homogeneity of the foil and a high counting rate of the fluorescence signal ensure a high signal-to-noise ratio. It is important to check that the normalization of the diffracted signal by I_0 suppresses any fluctuations in the incoming X-ray beam as a function of time and energy. Much effort must be paid to the optical alignment, and dynamic sagittal focusing and tuning of the second crystal of the monochromator are required in order to assure a smooth I_0 signal and beam stability as a function of energy. Also, one must check that the beam is well aligned through the centers of all sets of slits. All attenuators are to be located beyond the monitor so as not to perturb I_0 when they are inserted into the beam. It is preferable, however, not to use attenuators for measuring a DAFS spectrum. Regarding the detector and scattering slits, once the optimization of the Bragg diffraction has been achieved, a balance is struck between opening the slits enough to accept the divergence of the diffracted beam (with attention paid to the loss of resolution in the reciprocal space) and minimizing the fluorescence signal of the sample. A high signal-to-noise ratio is most easily obtained using flat samples which intercept the whole-diffracted beam. Additionally, flat samples are easier to correct for the effect of absorption, as described in §5.2.

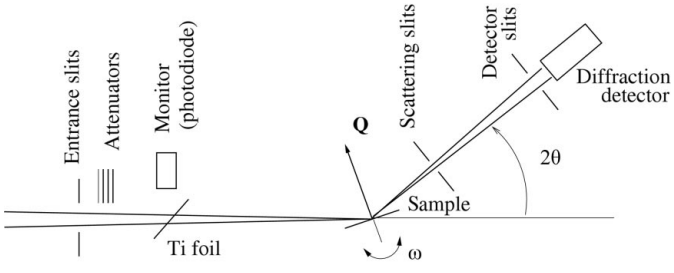

Figure 3
Schematic of the in-hutch portion of the diffraction set-up used to measure DAFS. Detailed information on detectors is given in §3.5.

For measuring a DAFS spectrum, either by measuring the maximum intensity or by integrating through the peak profile, one needs to track the Bragg peak as a function of the energy. For this, the intensity of the Bragg peak is carefully optimized at three or four points in the energy range of interest. Then a linear regression of sample position to energy is made to calculate the ω and 2θ angles throughout the energy scan. Note that the backlashes of all motors involved during a scan must be carefully checked and accounted for. As for an XAFS experiment, the linearity *versus* the energy of both detectors measuring the incoming and diffracted beams must be checked. As an example of typical data obtained with thin films or superlattices, Fig. 4 shows the DAFS spectra of a (001) superstructure reflection of a 50 nm-thick CoPt thin film, measured at the Pt $L_{\rm III}$ edge (Ersen, 2001).

3.4. Background subtraction

The energy-dependent background due to the fluorescence of the sample may not be negligible in the detector when measuring weak reflections. The use of energy-discriminating detectors to suppress the fluorescence is often not possible owing to their very low counting rates. A simple solution is to collect a spectrum off the Bragg peak and then to subtract it from the DAFS spectrum measured at the maximum intensity. However, a less time-consuming method is desirable. Wavelength-discriminating detection with a crystal analyzer is also used. For reasons of efficiency, an analyzer should have an angular acceptance comparable to the divergence of the diffracted beam and a reflectivity as high as possible. For this purpose, we used the (002) reflection of a flat graphite single crystal, the mosaicity of which is about 0.3° (FWHM). When measuring very low counting rates, care should be taken for all fluorescence emission lines; for instance, the K_β line that cannot be isolated from the elastic signal at the edge. It should be noted that the use of an analyzer crystal adds at least one extra motor movement to adapt the crystal angle as the X-ray beam energy is tuned. We have also carried out experiments at BM2-D2AM using the (222) reflection of an MgO crystal. Although the beam attenuation was about 40 in comparison with the intensity measured without a crystal, we were able to measure DAFS spectra of the weak forbidden reflections (002) and (006) of a Fe_3O_4 single crystal at the Fe K edge (García *et al.*, 2000). Graded lattice-spacing multilayers are good candidates because of

their large angular acceptance and high reflectivity. A further alternative is dynamic background subtraction. As described above in §3.1, it is possible to measure the derivative of the Bragg peak profile; therefore the constant background, including the fluorescence signal of the sample, is readily eliminated. A double integration of the derivative signal gives back the integrated intensity over the background (Coraux, 2000).

3.5. Detectors

In order to cope with and to benefit from the high counting rate on the I_0 detector, the sample fluorescence or the diffraction peak, we have developed a detector based on photodiodes operating in photovoltaic mode at room temperature which provides high linearity and a very large dynamic range. On the other hand, photodiodes have a high quantum efficiency (about 4 eV is necessary to create an electron–hole pair in Si) and a very low background can be achieved, allowing X-ray photons to be counted down to few thousand per second at 10 keV. These are PIN silicon photodiodes (Canberra-Eurysis, PD 300-15-300 CB) with an active area diameter of 19.5 mm, 300 μm thick, and covered with a 50 nm-thick aluminium entrance window. The surface orientation is [111] with a miscut of 7°. Fig. 5 shows our photodiode-based detector. For practical convenience the external design is the same as a scintillator detector. There is no metal or ceramic support right on the back of the active area and the electric connections on the silicon are shielded. A 10 μm-thick aluminium foil prevents illumination of the photodiode by visible light. High-purity aluminium foil (99.999%) is used to avoid signal contamination by trace elements such as iron or iron oxide, although high-purity Be windows would be an attractive alternative for low-energy DAFS. To connect the photodiodes to the electrometer, we use low-noise tri-ax cables (Keithley SC22) as short as possible to limit current fluctuations (maximum length 1 m). Consequently, the electrometer for measuring the diffracted beam is mounted on the 2θ arm. The photocurrent is measured using a NOVELEC electrometer (EC-PV High Sensitivity) with current scales ranging from 10^{-10} to 3×10^{-7} A. The V/F converter starts at 10^6 Hz (up to 10^7 Hz) to ensure linearity of the V/F conversion at very low voltage, allowing a precise compensation of the leakage current. The leakage current is lower than 10^{-12} A and can barely be detected. Most important, the dark-current signal-to-noise ratio is about 10^4. Owing to temperature variations in the experimental hutch, however, the dark current can fluctuate with an amplitude lower than $\pm 5 \times 10^{-13}$ A on a time scale of a few hours. Therefore a periodic measurement of the dark current is performed during the data acquisition when measuring in the most sensitive range (10^{-10} A). A further development will be inserting a chopper into the beam (with a frequency of few tenths of a Hz) and performing a synchronous detection to remove the dark current.

These detectors have a very large dynamic range, starting from 1000 counts s^{-1} up to the actual upper limit given by the highest scale (3×10^{-7} A), corresponding to about 9×10^8 counts s^{-1} at 10 keV. Although the photodiodes are well suited to a typical DAFS experiment, multiple diffraction inside the photodiode might be excited. This would be true in a case where the diffracted beam has a very small divergence, comparable to that of the perfect Si crystal.

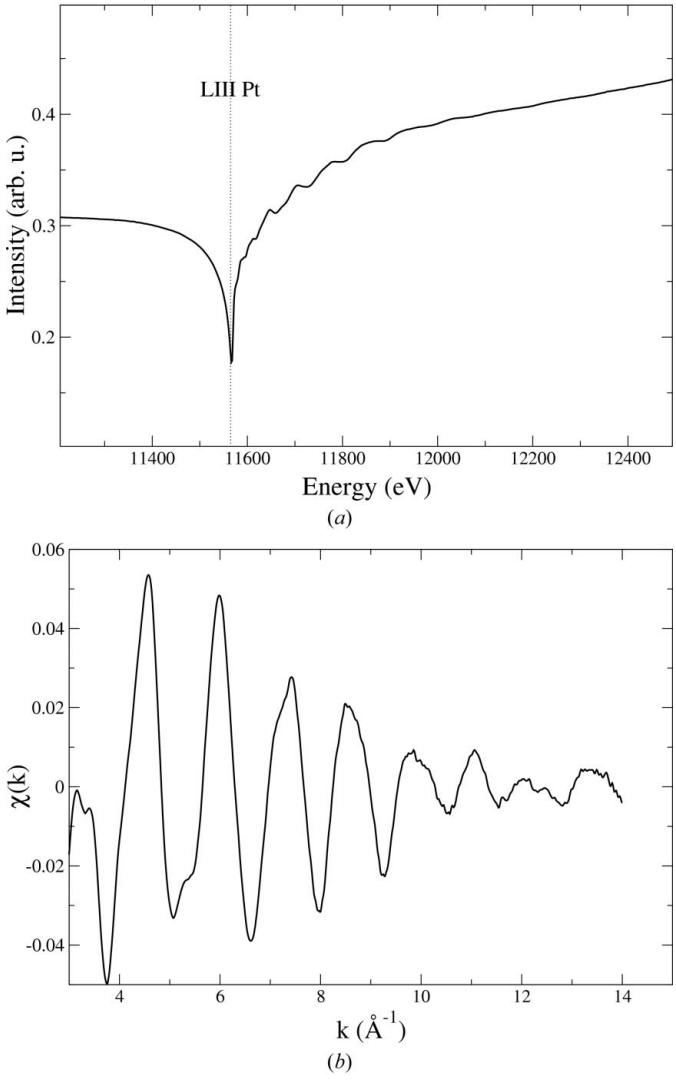

Figure 4
(*a*) Raw DAFS spectrum I_d/I_0 of the (00l) superstructure reflection of a 50 nm-thick CoPt thin film, measured around the Pt L_{III} edge. (*b*) The EDAFS spectrum normalized to I_s, where I_s is the diffracted intensity without oscillations.

4. Quick DAFS

Currently, the data-collection time for an energy-scanned experiment is rather long, of the order of one or a few hours. This is mainly due to the dead time required to move the sample and monochromator motors and is not due to the counting time which is often as short as a few seconds. To address this, we have implemented a quick-DAFS (q-DAFS) procedure that allows counting during motor movements. Quick-EXAFS has been used for more than a decade, since the pioneering work of Frahm (1988), and a 1 keV-range quick-EXAFS

Figure 5
The photodiode-based detector used for measuring DAFS spectra. The dimensions are the same as for common scintillator-based detectors, allowing the use of off-the-shelf detector mounts.

spectrum is typically obtained in a few seconds. A q-DAFS experiment is more complicated since at least three motors need to be moved: the monochromator, ω and 2θ. Here we show how we have achieved a 1 keV-range q-DAFS spectrum in a few minutes, as compared with about 1 h for a step-by-step scan. The principle is to use the pulses generated by the monochromator stepper motor to trigger the stepper motion of the other motors as well as the counting crate in order to have perfect synchronization. The angular speed of the monochromator ($d\omega_{mono}/dt$) is related to the ω motor speed of the diffractometer ($d\omega/dt$) by

$$\frac{d\omega_{mono}}{dt} = \frac{d\omega}{dt}\left[\frac{(\Gamma_{mono}E)^2-1}{(\Gamma_{sample}E)^2-1}\right]^{1/2}, \quad (5)$$

where $\Gamma = 2d_{hkl}/hc$ and E is the energy of the incoming beam ($\Gamma = 2d_{hkl}$ [Å]/12.398). Equation (5) shows that the angular speeds are related *via* a non-linear expression, except when $\Gamma_{sample}E \gg 1$ and $\Gamma_{mono}E \gg 1$, *e.g.* at high energy. This difficulty is solved with the programmable VPAP (VME-PAP: VERSA Module Eurocard-PAP) crates that drive the stepper motors and allow arbitrary synchronization of the motor movements. The monochromator motor is launched with a given angular speed from the initial to final ω_{mono} values. The ω and 2θ motors move, one and two steps, respectively, in the forward direction according to Bragg's law when a tabulated number of pulses from the monochromator motor are intercepted by the VPAP crates. We also synchronize the movement of a few other motors as a function of the energy to dynamically focus the beam in the horizontal plane and to tune the monochromator second crystal. Every pulse from the monochromator motor triggers the reading of the counting crate. The actual minimum angular step of that motor is 0.0002°. With a monochromator angular speed of 100 steps s^{-1}, a reading is made every 10 ms and about every 0.05 eV at the Ga *K* edge (10.367 keV). This means that 200 s are needed to measure a DAFS spectrum over a 1000 eV range. This hardware-based procedure ensures a perfect synchronism of all motors and counting and can also be used with the feedback control described in §3.1. The angular speed of the monochromator depends on the number of diffracted photons per second, and should be adapted accordingly to obtain an appropriate counting statistic. It also depends on the time response and efficiency of the sample rocking-angle feedback. We have tested the q-DAFS with a GaAsP thin film grown on a GaAs substrate. Fig. 6(*a*) shows the DAFS spectrum of the (006) reflection of the GaAsP film, measured in 4 min, with the feedback control on, and Fig. 6(*b*) shows the EDAFS extracted using the program *autobk* (Newville *et al.*, 1993) and the formula $(I_{meas} - I_s)/I_s$, where I_s corresponds to the diffracted intensity without oscillations. The FWHM of the rocking scan was 0.02°. Similar spectra, reported by Proietti *et al.* (1999), were obtained using the standard step-by-step energy scan and by measuring the maximum intensity, without feedback, in about 1 h per scan. Indeed, the q-DAFS procedure gives spectra of similar quality in a much shorter time. With the feedback control it was also possible to measure the q-DAFS spectrum of the very narrow (006) reflection (FWHM = 0.008°) of the GaAs substrate, shown in see Fig. 6(*c*).

5. Data reduction for EDAFS analysis

5.1. Diffraction intensity

For any crystallographic structure, the structure factor may be written as (Proietti *et al.*, 1999)

$$F(\mathbf{Q}, E) = \left\| F_T(\mathbf{Q}, E) \right\| \exp\left[i\varphi_T(\mathbf{Q})\right] + \sum_{j=1}^{N_A} \alpha_{Aj}(\mathbf{Q}) \exp\left[i\varphi_{Aj}(\mathbf{Q})\right]\left(f'_{Aj} + if''_{Aj}\right)(E). \quad (6)$$

The summation runs over all anomalous atoms in the unit cell, N_A, $\mathbf{Q}$ is the scattering vector and E is the energy of the incident beam.

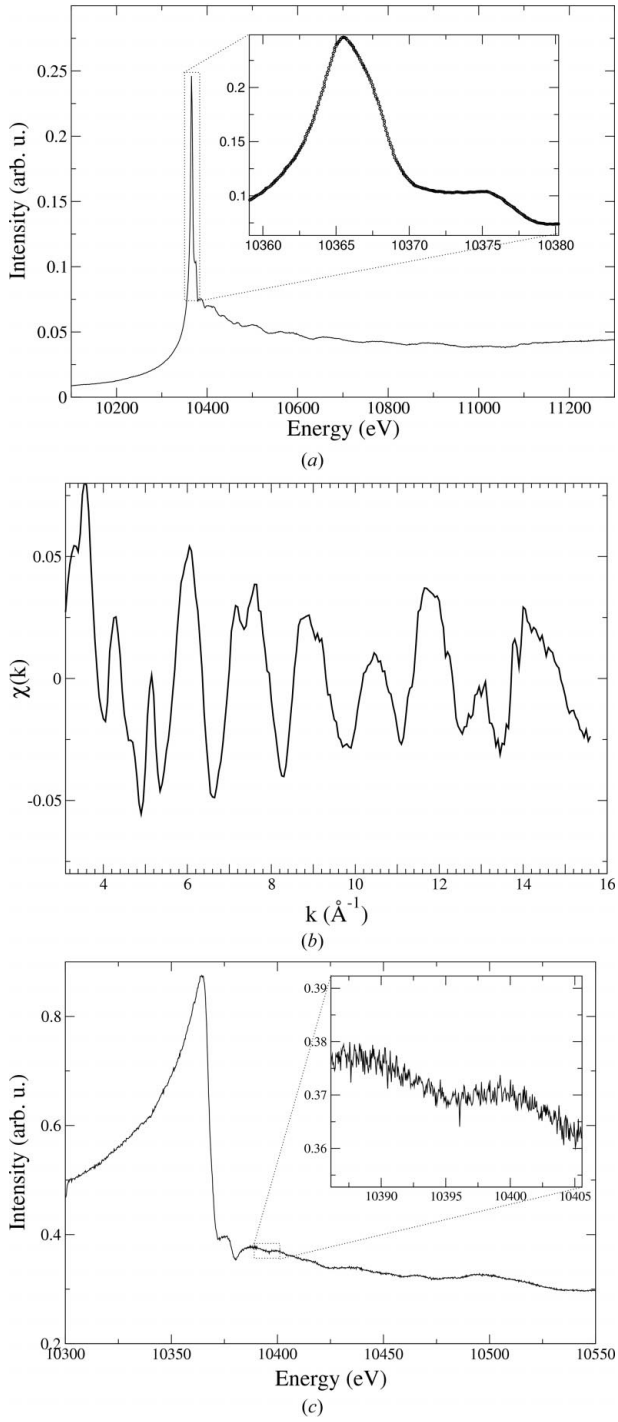

Figure 6
(*a*) q-DAFS spectrum of the (006) reflection of a GaAsP film, measured in 4 min using the feedback control described in §3.1. (*b*) EDAFS of the (006) reflection of the GaAsP file, normalized to I_s. (*c*) q-DAFS spectrum of the (006) reflection of a GaAs substrate, with the feedback control. The FWHM of the substrate peak was 0.008°. Insets show the signal quality in terms of sampling (0.05 eV step) and signal-to-noise ratio.

F_T is a complex structure factor of phase φ_T which includes the overall contribution of all non-anomalous atoms and the Thomson scattering of all anomalous atoms, $\alpha_{Aj} = c_{Aj}\exp(-M_{Aj}Q^2)$ and $\varphi_{Aj} = \mathbf{Q}\cdot\mathbf{r}_{Aj}$ is the scattering phase of atom A on site j. Then it can easily be shown that

$$\left\|F_0(\mathbf{Q},E)\right\|^2 = \left\|F_T\right\|^2\left\{\left[\cos(\varphi_T-\varphi_A)+\beta f'_{0A}\right]^2 + \left[\sin(\varphi_T-\varphi_A)+\beta f''_{0A}\right]^2\right\}, \quad (7)$$

where $F_0(\mathbf{Q},E)$ is the smooth non-oscillatory part of the complex structure factor and $\varphi_0(\mathbf{Q},E)$ is its phase, calculated assuming that the anomalous corrections (f'_{0A}, f''_{0A}) are identical for all anomalous atoms in the EDAFS region, $\beta = ||\alpha_A||/||F_T||$ and $||\alpha_A||\exp(i\varphi_A) = \sum_{j=1}^{N_A}\alpha_{Aj}\exp(i\varphi_{Aj})$. The decomposition of $F_0 = ||F_T||\exp(i\varphi_T) + ||\alpha_A||\exp(i\varphi_A)(f'_{0A}+if''_{0A})$ in the complex plane is shown in Fig. 7. Equation (7) shows that the energy-dependent variations of the diffracted intensity near an absorption edge give access to the phase difference $\Delta\varphi = \varphi_T - \varphi_A$ and the ratio β, and therefore gives precise information on the long-range average crystallographic structure, *i.e.* on atomic displacements and concentration of the anomalous atoms. The smooth part of a DAFS spectrum can be simulated by equation (7), although there may be some discrepancy at the edge for weak reflections if different anomalous sites exist with energy-shifted (also known as chemically shifted) anomalous factors. Apart from recovering the crystallographic parameters $\Delta\varphi$ and β, equation (7) is used to verify the absence of gross data distortions throughout the energy range. Equations (6) and (7) can be easily generalized to the case of two or more chemically shifted resonant atoms or to the case of atoms with different atomic numbers but nearby resonant energies (Ravel *et al.*, 1999).

A DAFS spectrum is related to the squared modulus of the structure factor after several corrections and according to the following formula,

$$I_{bs} = I_{meas} - I_{bgd} = r_0^2 S(\mathbf{Q})A(\mathbf{Q},E)D(E)(1/\sin\theta)L(\mathbf{Q},E)P(\mathbf{Q})\left\|F(\mathbf{Q},E)\right\|^2, \quad (8)$$

where I_{bgd} is the background intensity, including fluorescence or diffuse scattering, r_0 is the classic electron radius, S is a scale factor, A is the absorption correction, D is the detector efficiency, L and P are the Lorentz and polarization factors for the Thomson scattering, respectively, and $1/\sin\theta$ takes into account the variation of the size of the beam footprint on the sample surface when changing the incident angle (it is assumed that the beam footprint is smaller than the sample size). The D factor takes into account the whole detection set-up, comprising the detector efficiencies and the absorption all the way from the monitor to the diffraction detector. The value of D can be obtained by making a base-line measurement of the direct beam as a function of energy. It turns out that the energy dependence of this factor is linear inside the energy range of interest and so D may be fitted to the DAFS data with a straight line $[D = (m\Delta E + 1)]$, where m is the only adjustable parameter, $\Delta E = E - E_0$, and E_0 is the energy at the edge. In that case, care should be taken to measure the DAFS spectrum far enough from the absorption edge up to the point where anomalous effects are negligible, otherwise the m parameter will be correlated to the crystallographic phase $\Delta\varphi$. It is always recommendable to measure a base-line, then the D factor is readily recovered. For a rotation scan, *i.e.* with the rotation axis perpendicular to the plane of incidence (containing $\mathbf{k}$ and $\mathbf{k}'$), $L = \lambda^3/\sin 2\theta$, and the polarization correction for the Thomson scattering is given by the dot product $\boldsymbol{\varepsilon}\cdot\boldsymbol{\varepsilon}'$, where $\boldsymbol{\varepsilon}$ and $\boldsymbol{\varepsilon}'$ are the polarization vectors of the incoming and outgoing photons, respectively. If the electric field is perpendicular to the plane of incidence (σ–σ scattering), the polarization factor is $P = p + (1-p)\cos^2 2\theta$, where p is the σ polarization rate. $P = p\cos^2 2\theta + (1-p)$ when the electric field is in the plane (π–π scattering). At a bending magnet, the polarization of the incoming beam is almost entirely linear and p is close to unity (95% at beamline D2AM). For different geometries, see the *International Tables for Crystallography* (Wilson & Prince, 1999).

Normalization of the EDAFS oscillations can readily be obtained by multiplying the extracted signal $[I_{bs}/A(\mathbf{Q},E) - I_s]/I_s$ (where I_s corresponds to the diffracted intensity, corrected for absorption, without oscillations) by (Proietti *et al.*, 1999)

$$S_D = \left\{\left[\cos(\varphi_T-\varphi_A)+\beta f'_{0A}\right]^2 + \left[\sin(\varphi_T-\varphi_A)+\beta f''_{0A}\right]^2\right\}^{1/2}/(2\beta\Delta f''_{0A}).$$

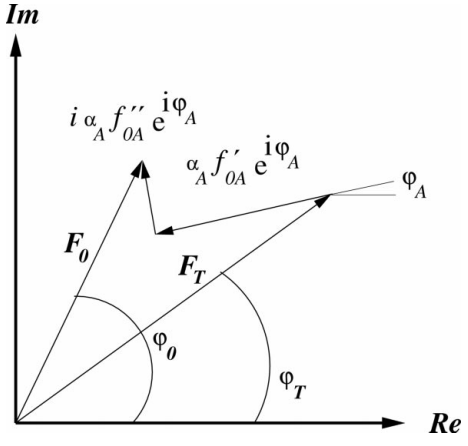

Figure 7
Representation of the structure factor $F_0(\mathbf{Q},E)$ in the complex plane (see text).

5.2. Absorption correction

Absorption is a concern for DAFS spectroscopy because it introduces significant structure at the edge that is strongly correlated to $\Delta\varphi$ and can introduce distortions to the EDAFS oscillations. Therefore it is important to evaluate the effect of absorption before measuring a DAFS spectrum. In this section we discuss data reduction and show how to correct for absorption and to minimize its effect by proper measurement strategy. We recall the general expression which represents the absorbed intensity for an incident beam impinging on a flat sample of thickness t, in reflection geometry, with the diffraction vector perpendicular to the surface (symmetric reflection),

$$A(\mathbf{Q},E) = \int_0^t \exp(-2\mu z/\sin\theta_B)\,dz = \frac{1-\exp(-2\mu t/\sin\theta_B)}{2\mu/\sin\theta_B}, \quad (9)$$

where μ [m^{-1}] is the absorption coefficient, θ_B is the Bragg angle and the factor 2 in the exponential takes into account the absorption by both the incident and diffracted beams. Equation (9) applies only to symmetric reflection; for other reflection geometries see the *International Tables for Crystallography* (Wilson & Prince, 1999). If the film thickness is small enough that $2\mu t/\sin\theta_B \ll 1$, then $A \to t$, a constant. For a bulk sample, $A = \sin\theta_B/2\mu$, and the absorption effect is strong. The correction to anomalous diffraction data affected by strong absorption has been studied, for instance, by Vacínová *et al.* (1995), Bos (1999) and Bernhoeft (1999). In the case of an almost perfect crystal and strong reflection, Meyer *et al.* (2003) have given a quantitative approach to correct for secondary extinction. In prin-

Table 1
$||\alpha_A||$, $||F_T||$, β and $\Delta\varphi$ values for the (004) and (006) reflections of InAs at the As K edge.

Calculations are performed at the As K edge (11.867 keV) and do not take into account the Debye–Waller factors ($M = 0$).

	$\|\alpha_A\|/4$	$\|F_T\|/4$	β	$\Delta\varphi$
(004)	1	55.06	0.018	2.6°
(006)	1	8.4	0.12	−162.4°

ciple, we need the true μ to calculate equation (9). The true μ, however, is not generally available. From equation (2), the absorption coefficient can be calculated in the forward-scattering limit,

$$\mu\ [\mathrm{m}^{-1}] = 2r_0(hc/E)N_T f_T''(E)\left[1 + \frac{N_A f_A''(E)}{N_T f_T''(E)}\right], \qquad (10)$$

where $\mu_{A,T} = N_{A,T}\sigma_{A,T}$ and N_T and N_A are the number of non-resonant and resonant atoms per m^3, respectively; f_T'' and f_A'' are measured in electron units. It can be also expressed as

$$\mu\ [\mathrm{cm}^{-1}] = \frac{69876.576}{E\ [\mathrm{keV}]\ V\ [\mathrm{\AA}^3]}\ N_T f_T''(E)\left[1 + \frac{N_A f_A''(E)}{N_T f_T''(E)}\right], \qquad (11)$$

where N_T and N_A are the number of non-resonant and resonant atoms in the unit cell, respectively, E is the energy of the incident beam in keV and V is the unit-cell volume in Å^3. Over a typically measured energy range, $f_T''(E)$ has a weak linear dependence on E and can be expressed in equations (10) and (11) as $f_T''(E) = f_T''(E_0)(m\Delta E + 1)$, where m is an adjustable parameter. If $N_A f_A'' \ll N_T f_T''$ in equation (11), then the absorption coefficient is a constant.

The imaginary part $f_A''(E)$ in equation (10) can be calculated either from the fluorescence spectrum, using for instance the software *DIFFKK* (Cross, Newville *et al.*, 1998) [note that in the case of strong absorption the fluorescence spectrum is distorted by self-absorption and corrections must be applied (Tröger *et al.*, 1998)], or from theoretical values. An experimental $A(\mathbf{Q}, E)$ can be obtained at a given $\mathbf{Q}$ by measuring the DAFS spectrum of a Bragg peak which is not sensitive to the anomalous atoms (*i.e.* the substrate or the buffer peaks or, if available, a reflection for which anomalous atoms have a negligible contribution). Then, experimental N_A, $N_T f_T''(E_0)$ and m can be recovered using equation (9) to fit the experimental $A(\mathbf{Q}, E)$, where N_A, $N_T f_T''(E_0)$ and m are adjustable variables. In this way one can recover the true absorption coefficient μ from the fluorescence signal spectrum and the absorption jump at the edge in a DAFS spectrum from an experimental $A(\mathbf{Q}, E)$. Note that when using the substrate or buffer peaks a constant equal to $[\sin(\theta_B)/2\mu_{sub}] \times \exp(-2\mu_{sub}t/\sin\theta_B)$ must be added to the thin-film absorption correction, where μ_{sub} is the substrate or buffer absorption coefficient.

Although absorption effects are often small when measuring thin films, this does not mean that there is no way of measuring bulk samples or that absorption is always negligible for thin samples. The relevant quantity is the absorption jump amplitude, given to first order by $2\mu t/\sin\theta_B$, relative to the anomalous effect. Equation (7) shows that the higher the parameter $\beta(\mathbf{Q})$ the higher the relative anomalous amplitude. High β values correspond to high $||\alpha_A||$ (*e.g.* all anomalous atoms are in phase) and small $||F_T||$. Almost systematically, weak reflections fulfill that criteria and occur when resonant and non-resonant atoms scatter out of phase. As an example, take two reflections of the zincblende-like InAs compound: the strong ($004 = 4n$) for which In and As scatter in phase, and the weak ($006 = 4n + 2$) for which In and As scatter out of phase. The values for β, $||\alpha_A||$ and $||F_T||$ are reported in Table 1 at the As K edge. Fig. 8 shows the (004) and (006) DAFS spectra calculated by using experimental f'_{As} and f''_{As} obtained from an XAFS spectrum of bulk InAs. The squared modulus of the structure factor has been multiplied by $A(\mathbf{Q}, E)/t$, calculated for a sample thickness t of one tenth of an absorption length at the edge ($t = 0.1/\Delta\mu \simeq 2.8$ µm, the variation $\Delta f''_{As}$ of f''_{As} at the edge is equal to 3.4). The (004) DAFS spectrum clearly exhibits an absorption-like shape, whereas the (006) reflection is much less affected.

We would also like to point out, without entering into detail [for EDAFS data analysis, see Proietti *et al.* (1999)], that a proper choice of the Bragg reflection can also help to minimize distortions to the EDAFS oscillations induced by absorption. The structure factor $F(\mathbf{Q}, E)$ can be split into its smooth and oscillatory parts, as in equation (5) of Proietti *et al.* (1999). The oscillatory behaviour of $A(\mathbf{Q}, E)$ propagates into the DAFS oscillations leading to distortions whose strengths depend on the relative amplitude of the absorption oscillations compared with the amplitude of the DAFS oscillations. To first order, $A(\mathbf{Q}, E)/t \simeq 1 - 2\mu t/\sin\theta_B$, then the relative oscillations amplitude of $A(\mathbf{Q}, E)$ scales as $2\mu_0 t/\sin\theta_B$, where $\mu = \mu_0(1 + \chi'')$. We observe in Fig. 8(*d*) that the distortion of the extended DAFS is negligible for the (006) Bragg reflection whereas it is strong for (004), shown in Fig. 8(*c*). It has to be

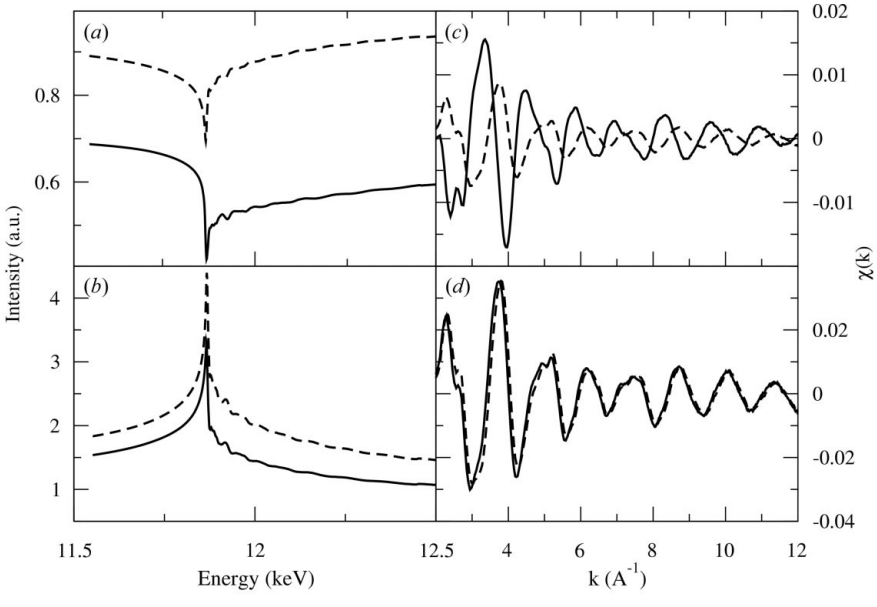

Figure 8
(*a*) DAFS spectra of the InAs (004) reflection, multiplied by $A(\mathbf{Q}, E)/t$ calculated with $t = 0$ [$A(\mathbf{Q}, E) = 1$] (dashed line) and $t = 2.8$ µm (one-tenth of an absorption length) (solid line). (*b*) Same as (*a*) but for the InAs (006) reflection. The total X-ray path length inside the sample, $2t/\sin\theta_B$, is about 19 µm for (004) and 11 µm for (006). (*c*) EDAFS oscillations of the InAs (004) reflection are strongly affected by absorption, whereas EDAFS oscillations of the InAs (006) reflection are not (*d*).

noted that amplitude contrast of the DAFS oscillations at the first order is weighted (Proietti *et al.*, 1999) by $||\alpha_A||/||F_0||$ and at the second order by $||\alpha_A||^2/||F_0||^2$, *i.e.* not weighted by the ratio $\beta = ||\alpha_A||/||F_T||$ as for the amplitude of the anomalous effect. Also, with a superlattice or very weak reflections, we could have a situation in which, despite a modest anomalous effect ($\beta \ll 1$), oscillations show a large relative amplitude owing to chemical shifts or polarization effects (ATS) that make anomalous sites inequivalent (Cross, Newville *et al.*, 1998; Toda *et al.*, 1998). Forbidden reflections are a limiting case where $||F_0|| = ||\alpha_A|| = 0$ and only DAFS oscillations owing to ATS contribute at the second order to the signal. This is by far the most favorable case where the relative absorption correction is the weakest; indeed, forbidden reflections of bulk samples (for which absorption is strong) can be measured and corrected [$A(\mathbf{Q}, E) = 1/\mu$] (García *et al.*, 2000; Renevier *et al.*, 2001).

Finally, we want to mention how the absorption correction should be taken into account in the case of anisotropy of the scattering factor. As stated in §2, absorption in non-cubic single crystals is not isotropic and depends on the polarization vector direction of the incoming beam with respect to the principal axis of the crystallographic point group. For instance, the absorption cross section does not depend on polarization in a cubic crystal whereas it does in a tetragonal crystal. Similarly, anomalous scattering is not a scalar quantity: it depends on the polarization vector directions of the incoming and outgoing beams with respect to the principal axis of the point-group symmetry of the resonant atoms (ATS). After summation over all resonant atoms A, the ATS may produce scattering in the σ–σ and/or σ–π channels. Strictly speaking, this means that only the σ–σ scattering (incoming and outgoing polarization vectors perpendicular to $\mathbf{Q}$) can be corrected with experimental absorption data measured either in transmission or fluorescence mode, provided that diffraction and absorption be measured with the polarization of the incident beam in the equivalent direction (Cross, Newville *et al.*, 1998) (see Fig. 9 for a schematic representation of both scattering channels). Regarding σ–π and π–π scattering, there is no easy experimental solution: one can measure two absorption spectra, one with the polarization vector parallel to the polarization vector of the incoming beam and the other parallel to that of the outgoing beam. The σ–π scattering, that originates from the off-diagonal terms of [D], has to be checked only for forbidden or very weak reflections, when the diagonal contribution almost cancels out. We wish to note that care must be taken with powder samples, since the absorption does not depend on polarization but the DAFS does (Bos, 1999).

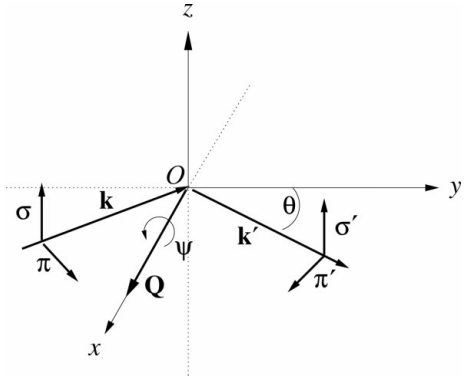

Figure 9
Schematic representation of the σ–π and σ–σ scattering geometries. (O, x, y) is the plane of incidence in the schematic representation.

6. Concluding remarks

The aim of this paper is to give an up-to-date general overview of the technical aspects of DAFS spectroscopy. We believe that this technique is underdeveloped compared with XAFS, despite providing significant measurement capabilities unavailable to XAFS. Along with chemical selectivity, DAFS offers spatial and site selectivity, allowing for the application of well established methods of XAFS data analysis to new classes of problems. In this sense we direct this paper to the XAFS community. We hope that we have demonstrated that, in spite of the relative complexity of a DAFS measurement compared with XAFS, significant progress has been made, making DAFS easier and more accessible.

We have thoroughly described the experimental set-up, paying attention to the requirements of the design of the mirrors and monochromator as well as to optical and sample alignment. These experimental practices are essential to the collection of high-quality data. We have also discussed issues of detector design and mounting relevant to high-quality data collection. We used silicon photodiodes with a large dynamic range able to cope with high X-ray fluxes and ensuring excellent signal-to-noise ratios on both the I_0 monitor and the diffraction detector comparable with XAFS measurements. We also noted the importance of obtaining a perfect monitor-corrected I/I_0 normalization along the whole energy scan.

Among the possible experimental schemes for performing energy-scan diffraction, we have focused on the maximum-intensity measurement procedure. It has been dramatically improved at BM2-D2AM by developing a feedback system that has proved to be very efficient in reducing measurement time and increasing the signal-to noise ratio. A further improvement to the DAFS technique at BM2-D2AM has been the development of q-DAFS combined with the feedback system. It allows collection of a DAFS spectrum in a few minutes. We have also treated the subject of absorption correction, a major concern in data reduction. We have shown how to use a fluorescence spectrum plus the jump at the edge of $A(\mathbf{Q}, E)$ to recover the true μ spectrum and to calculate the absorption-correction factor in a reliable way.

Finally, this paper provides information about the state of the art of the DAFS technique at beamline D2AM at the ESRF. We have tried to make the application of the DAFS spectroscopy more attractive to a wider section of the scientific community.

We acknowledge the French CRG for granting beam time and support to developing the DAFS spectroscopy at the beamline BM2-D2AM. One author (BR) is pleased to acknowledge post-doctoral fellowship support from the Centre National pour la Recherche Scientifique. We are grateful to Y. Joly, E. Lorenzo, G. Subias and J. Garcia-Ruiz for many helpful discussions and to the PhD students J. Vacínová, S. Bos and V. Favre-Nicolin for their contributions to the development of the DAFS spectroscopy. A special thanks to all users who have manifested interest in DAFS.

References

Arcon, I., Kodre, A., Glavic, D. & Hribar, M. (1987). *J. Phys. C (Paris)*, **9**, 1105–1108.
Arndt, U., Greenhough, T., Helliwell, J., Howard, J., Rule, S. & Thompson, A. (1982). *Nature (London)*, **298**, 835–838.
Bernhoeft, N. (1999). *Acta Cryst.* A**55**, 274–288.
Blanco, N. (1998). *Optimization de l'Intensité de Diffraction pour la Spectroscopie DAFS*. Rapport de Stage, Maîtrise de Physique et Applications, Université Joseph Fourier, Grenoble, France.
Blume, M. (1985). *J. Appl. Phys.* **57**, 3615–3618.
Bos, S. (1999). PhD thesis, Université Joseph Fourier, Grenoble, France.
Brouder, C. (1990). *J. Phys. Condens. Matter*, **2**, 701–738.

Cauchois, Y. (1956). *C. R. Acad. Sci. (Paris)*, **242**, 100–102.
Cohen-Tannoudji, C., Diu, B. & Laloë, F. (1973). *Mécanique Quantique*, Vol. II. Paris: Hermann.
Cohen-Tannoudji, C., Dupont-Roc, J. & Grynberg, G. (1988). *Processus d'Interaction Entre Photons et Atomes.* InterEditions/Editions du CNRS.
Coraux, J. (2000). *Tests de Nouvelles Procédures de Mesure avec un Amplificateur 'Lock-In' pour la Spectroscopie de Diffraction Anomale à l'ESRF.* Rapport de Stage, Maîtrise de Sciences Physiques, Université Joseph Fourier, Grenoble, France.
Cross, J., Elam, W., Harris, V., Kirkland, J., Bouldin, C. & Sorensen, L. (1998). *J. Synchrotron Rad.* **5**, 911–913.
Cross, J. O., Newville, M., Rehr, J. J., Sorensen, L. B., Bouldin, C. E., Watson, G., Gouder, T., Lander, G. H. & Bell, M. I. (1998). *Phys. Rev. B*, **58**, 11215–11225.
Cross, J. O., Newville, M., Sorensen, L. B., Stragier, H. J., Bouldin, C. E. & Woicik, J. C. (1997). *J. Phys. IV*, **7**(C2), 745–747.
Dmitrienko, V. (1983). *Acta Cryst.* A**39**, 29–35.
Ersen, O. (2001). PhD thesis, Université Louis Pasteur, Strasbourg, France.
Ferrer, J.-L., Simon, J.-P., Bérar, J.-F., Caillot, B., Fanchon, E., Kaïkati, O., Arnaud, S., Guidotti, M., Pirocchi, M. & Roth, M. (1998). *J. Synchrotron Rad.* **5**, 1346–1356.
Frahm, R. (1988). *Nucl. Instrum. Methods Phys. Res. A*, **270**, 578–581.
Fukamachi, T., Hosoya, S., Kawamura, T. & Hastings, J. (1977). *Phys. Rev. B*, **10**, 321–324.
García, J., Subias, G., Proietti, M., Renevier, H., Joly, Y., Hodeau, J., Blasco, J., Sanchez, M. & Bérar, J. (2000). *Phys. Rev. Lett.* **85**, 578–581.
Grenier, S. (2001). PhD thesis, Université Joseph Fourier, Grenoble, France.
Grenier, S., Proietti, M., Renevier, H., Gonzalez, L., Garcia, J. & Garcia, J. (2002). *Europhys. Lett.* **57**(4), 499–505.
Grenier, S., Toader, A., Lorenzo, J., Joly, Y., Grenier, B., Ravy, S., Regnault, L., Renevier, H., Henry, J., Jegoudez, J. & Revcolevchi, A. (2002). *Phys. Rev. B*, **65**, 180101–180104.
Hazemann, J., Nayouk, K. & De Bergevin, F. (1995). *Nucl. Instrum. Methods Phys. Res. B*, **97**, 547–550.
Hendrickson, W. (1985). *Trans. Am. Crystallogr. Assoc.* **21**, 11.
Hodeau, J., Favre-Nicolin, V., Bos, S., Renevier, H., Lorenzo, J. & Bérar, J. (2001). *Chem. Rev.* **101**, 1843–1867.
Meyer, D., Kupsch, A. & Paufler, P. (1998). *J. Synchrotron Rad.* **5**, 1275–1281.
Meyer, D., Richter, K., Seidel, A., Weigelt, J., Frahm, R. & Paufler, P. (2003). *J. Synchrotron Rad.* **10**, 144–147.
Murakami, Y., Kawada, H., Kawata, H., Tanaka, T., Arima, T., Moritomo, Y. & Tokura, Y. (1998). *Phys. Rev. Lett.* **80**, 1932–1935.
Newville, M., Livins, P., Yacoby, Y., Stern, E. & Rehr, J. (1993). *Phys. Rev. B*, **47**, 14126–14131.
Pickering, I. J., Sansone, M., Marsch, J. & George, G. N. (1993*a*). *J. Am. Chem. Soc.* **115**, 6302–6311.
Pickering, I. J., Sansone, M., Marsch, J. & George, G. N. (1993*b*). *Jpn. J. Appl. Phys.* **32**(2), 206.
Proietti, M., Renevier, H., Hodeau, J., Garcia, J., Bérar, J. & Wolfers, P. (1999). *Phys. Rev. B*, **59**, 5479–5492.
Ravel, B., Bouldin, C. E., Renevier, H., Hodeau, J.-L. & Berar, J.-F. (1999). *Phys. Rev. B*, **60**, 778–785.
Renevier, H., Hodeau, J., Wolfers, P., Andrieu, S., Weigelt, J. & Frahm, R. (1997). *Phys. Rev. Lett.* **78**, 2775–2778.
Renevier, H., Joly, Y., Garcia, J., Subias, G., Proietti, M. G., Hodeau, J. L. & Blasco, J. (2001). *J. Synchrotron Rad.* **8**, 390–392.
Sakurai, J. (1967). *Advanced Quantum Mechanics.* New York: Benjamin Cummings.
Salem, S. & Hall, V. (1980). *J. Phys. F*, **10**, 1627.
Sorensen, L. B., Cross, J. O., Newville, M., Ravel, B., Rehr, J. J., Stragier, H., Bouldin, C. E. & Woicik, J. C. (1994). *Resonant Anomalous X-ray Scattering: Theory and Applications*, edited by G. Materlik, C. J. Sparks and K. Fischer, pp. 389–420. Amsterdam: Elsevier Science/North-Holland.
Stragier, H., Cross, J. O., Rehr, J. J., Sorensen, L. B., Bouldin, C. E. & Woicik, J. C. (1992). *Phys. Rev. Lett.* **69**, 3064–3067.
Templeton, D. & Templeton, L. (1980). *Acta Cryst.* A**36**, 237–241.
Toda, T., Nogami, T., Yamasaki, K. & Soejima, Y. (1998). *J. Appl. Cryst.* **31**, 423–429.
Tröger, L., Arvanitis, D., Baberschke, K., Michaelis, H., Grimm, U. & Zschech, E. (1998). *Phys. Rev. B*, **46**, 3283–3289.
Vacínová, J., Hodeau, J. L., Wolfers, P., Lauriat, J. P. & ElKaim, E. (1995). *J. Synchrotron Rad.* **2**, 236–244.
Wilson, A. & Prince, E. (1999). Editors. *Internationnal Tables for Cristallography*, Vol. C. Dordrecht: Kluwer.